Higher-order scene statistics of breast images

Craig K. Abbey[a,b], Jascha N. Sohl-Dickstein[c], Bruno A. Olshausen[c,d], Miguel P. Eckstein[a,e], and John M. Boone[b,f]

[a]Dept. of Psychology, University of California, Santa Barbara, USA;
[b]Dept. of Biomedical Engineering, University of California, Davis, USA;
[c]Redwood Center for Theoretical Neuroscience, University of California, Berkeley, USA;
[d]School of Optometry, University of California, Berkeley, USA;
[e]Institute for Collaborative Biotechnology, University of California, Santa Barbara, USA;
[d]Dept. of Radiology, UC Davis Medical Center, Sacramento, USA;

ABSTRACT

Researchers studying human and computer vision have found description and construction of these systems greatly aided by analysis of the statistical properties of naturally occurring scenes. More specifically, it has been found that receptive fields with directional selectivity and bandwidth properties similar to mammalian visual systems are more closely matched to the statistics of natural scenes. It is argued that this allows for sparse representation of the independent components of natural images [Olshausen and Field, *Nature*, 1996]. These theories have important implications for medical image perception. For example, will a system that is designed to represent the independent components of natural scenes, where objects occlude one another and illumination is typically reflected, be appropriate for X-ray imaging, where features superimpose on one another and illumination is transmissive?

In this research we begin to examine these issues by evaluating higher-order statistical properties of breast images from X-ray projection mammography (PM) and dedicated breast computed tomography (bCT). We evaluate kurtosis in responses of octave bandwidth Gabor filters applied to PM and to coronal slices of bCT scans. We find that kurtosis in PM rises and quickly saturates for filter center frequencies with an average value above 0.95. By contrast, kurtosis in bCT peaks near 0.20 cyc/mm with kurtosis of approximately 2. Our findings suggest that the human visual system may be tuned to represent breast tissue more effectively in bCT over a specific range of spatial frequencies.

Keywords: Breast imaging, natural scenes, kurtosis.

1. INTRODUCTION

X-ray imaging of the breast, most commonly performed as a projection mammogram, has been the clinical standard used to screen asymptomatic women for early signs of breast cancer. While it is now widely recognized that the technique is effective, there remains a substantial effort to improve the accuracy of the screening process. One of the principle limitations of mammography is the masking properties of normal anatomy in mammography. This general phenomenon has been recognized in medical imaging for many years [1-3]. More specific to mammography, research over the last 10 years has shown masking by normal anatomy to be the limiting factor for detecting masses [3,4].

The work of Burgess and colleagues [4,5] has shown that anatomy in projection mammography is well modeled by a power-law power spectrum, with additional power at higher spatial frequencies from acquisition noise. The power-law power spectrum of mammograms is consistent with a large body of literature on natural scenes [6-8]. Notably, exponents of power-law spectrum in mammography [4] are typically distributed around an average value of 2.8, which is somewhat higher than what is found for photographs of natural scenes. Power-law analyses have been extended to other forms of breast imaging such as tomosynthesis [9] and dedicated breast CT [10], both of which show reduced exponents in the power law.

Power spectra are inherently limited to second-order moments. Since random Gaussian images generated with an identical power spectrum are easily distinguished from patient mammograms, second order moments alone do not fully

Medical Imaging 2009: Image Perception, Observer Performance, and Technology Assessment,
edited by Berkman Sahiner, David J. Manning, Proc. of SPIE Vol. 7263, 726317

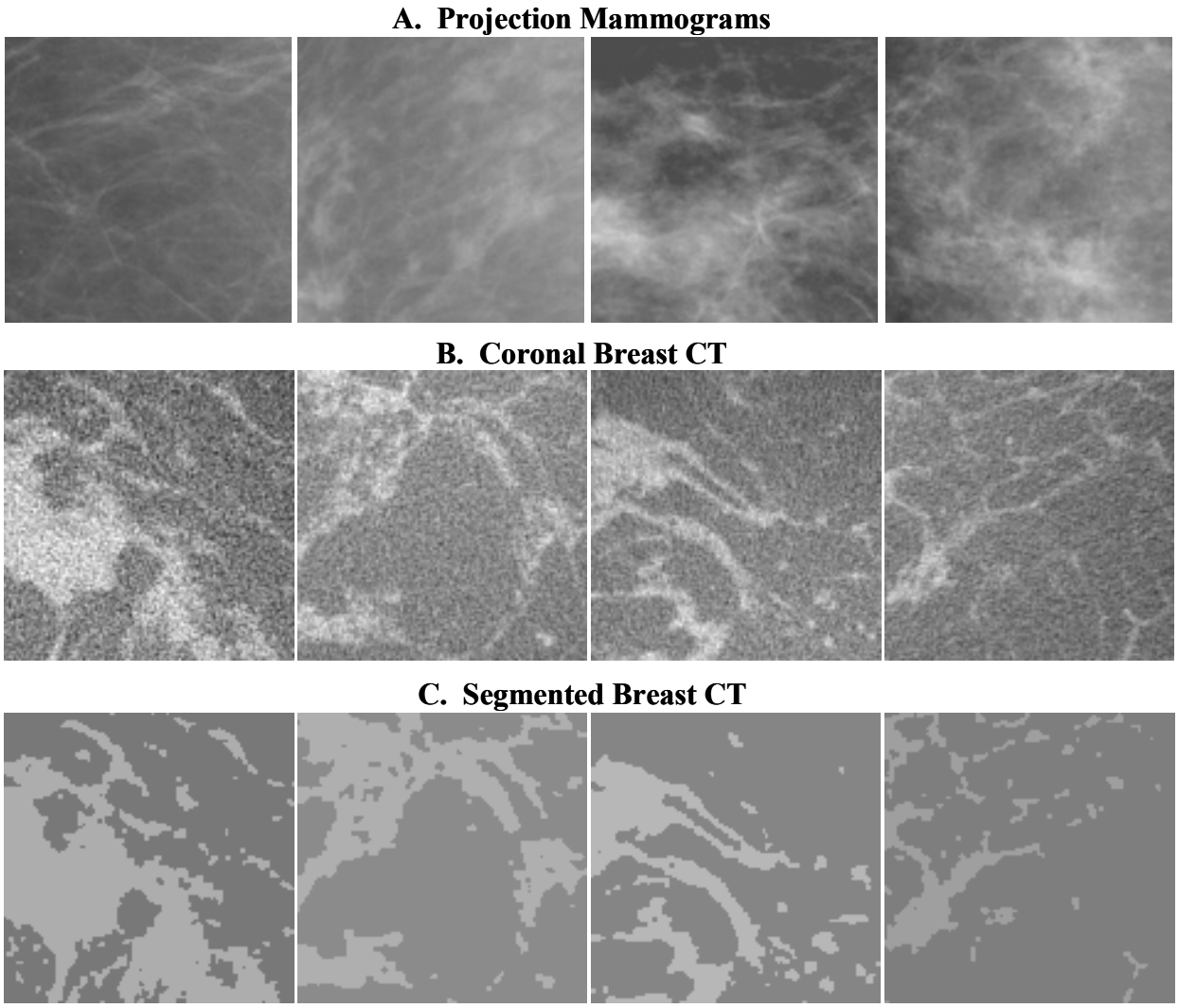

Figure 1. Examples of breast image ROIs. Four image ROIs taken from mammograms (A), coronal breast CT images (B), and segmentations of the CT images (C) are shown. The patches are rendered approximately at their physical size.

capture the statistics of anatomy in mammograms. Furthermore, higher-order statistics, not captured in a power spectrum, are likely to aid visual tasks relative to a Gaussian assumption. Burgess' study [4] shows that contrast thresholds for mammographic backgrounds are significantly lower than a Gaussian distribution matched in power spectrum, and have a less steeply sloped CD diagram. However, little is known about the statistical moments of breast images beyond second order. The purpose of this work is to investigate higher-order statistical properties of breast images, specifically the kurtosis of linear filters applied at random locations in an image.

The approach we take is based on methods from research in natural scene statistics, where investigators in the fields of visual neuroscience and computer vision are increasingly turning to higher order statistics of images to motivate models of the human visual system. In the first study, we evaluate the kurtosis of octave-bandwidth Gabor filters, with response properties very similar to linear models of receptive fields in the early visual system. We consider projection mammograms as well as coronal breast CT (bCT) images to give a sense of the differences in going from a 2D to a 3D imaging system. We also derive filters from these medical images using an approach pioneered by Olshausen and Field [11-13], who found filter-banks resembling visual receptive fields emerged in basis sets that enforced sparse (i.e. high-kurtosis) responses. The finding that receptive field responses have excess kurtosis suggests that these derived filters are more appropriate for describing the statistics of anatomy in projection mammography and bCT images [14].

2. THEORY

2.1 Variability in breast images

Figure 1 shows sample image patches from projections mammograms, coronal bCT images, and segmentations of the coronal bCT images. The patches are rendered at approximately the same physical size in all cases. These illustrate the texture of the different imaging modalities. The segmented bCT images are included in some of the analysis as an idealization of breast tissue absent any blurring or acquisition noise, consisting only of discrete labels for adipose and glandular tissue.

Part of the rationale for looking at higher-order statistics is based on the idealized notion of source recovery [11,14]. Here, images are thought of as a mixing of non-Gaussian sources. In the case of breast imaging, sources could be the location and shape of glands, ducts, vasculature, and other anatomical structures that can be appreciated in Figure 1. When the imaging process additively combines (or mixes) these structures together, the central limit theorem leads to a Gaussian distribution in most linear filter responses. However, filters that capture a single or small number of sources will retain a non-Gaussian distribution.

2.2 Kurtosis of filter responses

We use a measure of excess kurtosis, the ratio of the 4th-order moment to the square of the variance, to measure the deviation from Gaussian of the observed filter responses. Let x be a random variable with mean μ and variance σ^2. The excess kurtosis is defined as

$$\gamma = \frac{\left\langle (x-\mu)^4 \right\rangle}{\sigma^4} - 3 , \tag{1}$$

where the angle brackets indicate the expected value of the random quantity inside. The subtraction of 3 means that the excess kurtosis of a Gaussian will be zero. Note that Eq. (1) is often taken as the definition of kurtosis, making no distinction between kurtosis and excess kurtosis. We will use the two terms interchangeably.

Let x_k (k = 1, K) be a set of 2D filter responses for a filter $f[i,j]$ (where $i = 1, N_1 - 1$, and $j = 0, N_2 - 1$), acting on random locations within an image $g[i,j]$ (where $i = 1, M_1 - 1$, and $j = 1, M_2 - 1$). The filter response, x_k, for a filter located at position $[i_k, j_k]$ within the image is given by

$$x_k = \sum_{i=0}^{N_1-1} \sum_{j=0}^{N_2-1} f[i,j]\, g[i_k - N_1/2 + i, j_k - N_2/2 + j] . \tag{2}$$

In this case, the randomness in the filter responses is a consequence of random filter locations $[i_k, j_k]$.

Kurtosis of the filter responses is computed by replacing the expected quantities in Eq. 1 by sample estimates. Let $\bar{x}$ be the sample average, and $\hat{s}^2$ be the sample variance, the estimated kurtosis is computed as

$$\hat{\gamma} = \frac{1}{N\hat{s}^2} \sum_{k=1}^{K} (x_k - \bar{x})^4 - 3 . \tag{3}$$

2.3 Gabor-function filters

Gabor filters have attractive properties for use in a study of higher-order moments of images. They are relatively well-localized in both the spatial and spatial-frequency domains. They can also be tuned to spatial frequency, orientation, and bandwidth. Gabor functions are often used as a model of receptive fields in the early visual system, implying that the statistics of Gabor filter outputs are relevant in early visual processing.

We use sine-phase Gabors in this work. The critical parameters of the Gabor are the sine-wave center-frequency, f_0, and the width of the Gaussian envelope σ. Note that we use isotropic envelopes, and hence $\sigma_x = \sigma_y = \sigma$. The Gabor function is defined by

$$G(x, y; f_0, \sigma) = \sin(2\pi f_0 x)\, e^{-\frac{1}{2\sigma^2}(x^2+y^2)} , \tag{4}$$

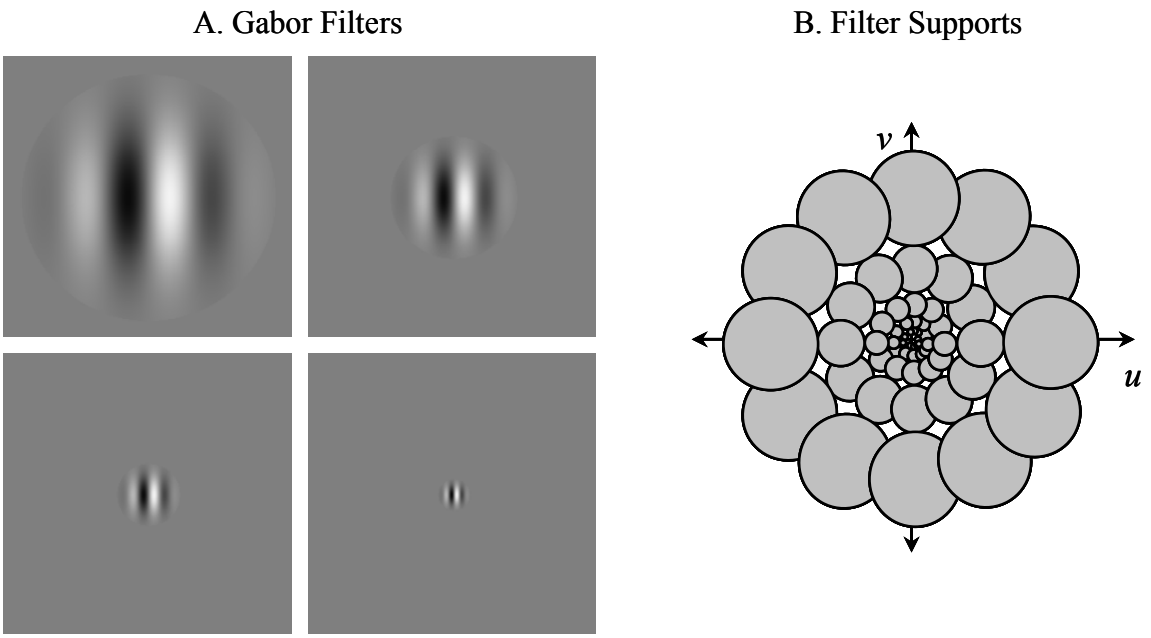

Figure 2. Gabor filters. The profiles (A) for a subset of (vertically) oriented octave-bandwidth Gabor filters with sine phase are shown along with a schematic illustration (B) of the 2D spectral support of the filters at all six orientations. Note the increasing support size at increasing distances from the origin in the frequency plane, which results in octave bandwidth across frequencies.

with translation and rotation implemented through coordinate transforms of this function.

We will use octave bandwidth Gabor filters, which specifies a particular relationship between f_0 and σ. The bandwidth in octaves is defined as $\log_2$ of the ratio of the lowest frequency of the filter spectrum to the highest. For Gabor functions, which have a smooth roll off, the high- and low-frequency limits are typically taken at the half-max points. The distance in the frequency domain from the center-frequency to the half-max point is $\sqrt{2\ln(2)}/2\pi\sigma$ in either direction. Thus the bandwidth of the Gabor is defined as $B = \log_2\left(f_0 + W / f_0 - W\right)$. Constraining B to 1 specifies the envelope width as a function of the center frequency,

$$\sigma = \frac{\sqrt{2\ln(2)}}{2\pi f_0}. \tag{5}$$

Note that Equation 5 implies that the spatial envelope of the Gabor gets wider as the center frequency gets lower (i.e. smaller f_0). Figure 2 gives examples of octave bandwidth Gabor filters and shows schematically how they cover the frequency domain with six different angular orientations.

2.4 Evolved filters using SparseNet

As an alternative to specifying a functional form for the filters as in the Gabor filters, we explore filters that emerge from the dual considerations of representing image data and imposing that the representation be sparse [11]. Here sparsity means that the majority of filter responses are near zero, with a small number of filters giving high-amplitude responses. Olshausen and colleagues have developed software implementing an iterative approach to finding sparse basis sets. A full description is beyond the scope of this proceedings paper, but details can be found publications related to the software [11-13].

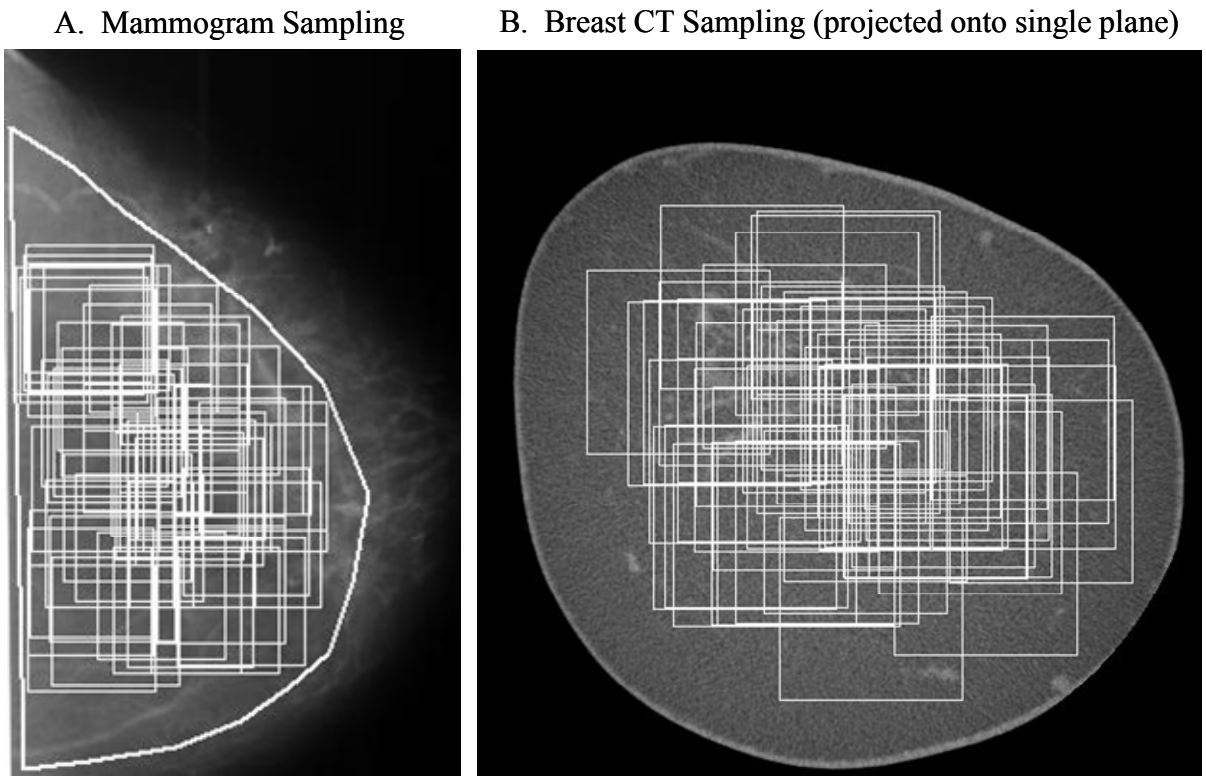

Figure 3. Region of interest (ROI) sampling of images. Location of 50 ROIs in projection mammograms (A) and coronal breast CT images (B). ROIs are confined to the interior of the breast by a manually drawn border in the case of mammograms and by use of the segmented image in the case of breast CT. Note that the ROIs in breast CT are also randomly located in depth and projected onto a single image for visualization.

3. MATERIALS AND METHODS

3.1 Sources of images

For projection mammography, we had access to a large set of projection mammograms that had been digitized from film. Some of these scans were originally used to investigate breast density by Boone and colleagues [15]. For consistency, only images made from digitized film of normal left breasts in the cranio-caudal view were used. Of these, we subselected 79 images based on the size of the interior region, as defined by the manual procedure described below. Only scans with at least 80 cm^2 of interior region were used in the analysis. The films were digitized at a resolution of 50 μm, and then downsampled to 250 μm (additional downsampling was used in the Boone *et al.* publication [15]). Output of the digitizer was converted to exposure by use of a calibrated lookup table, and then log-transformed to form an estimate of integrated attenuation through the compressed breast.

A total of 44 three-dimensional bCT images of the left breast were obtained from a dedicated cone-beam scanner developed by Boone and colleagues [16-18]. The image data used in this study was described more fully in a recent publication [10]. For each scan, 500 projection images were obtained at 80 kVp with a variable mAs set to match the dose of a two view mammogram of the same breast [17]. These images were acquired around the breast for 360^o coverage with some excess angular coverage used as a safeguard in the event of patient motion. Three-dimensional images were reconstructed by filtered backprojection with a Shepp-Logan filter [19, 20]. Transaxial (coronal) images encompassed 512 by 512 pixels, with a section thickness of 0.21 mm. The sixe of pixels in the coronal images varied across patients with an average of 0.34mm (range: 0.23mm to .41mm; coefficient of variation 11.3%).

Segmented breast CT images were generated using an algorithm developed specifically for bCT data [21, 22]. The algorithm segments the scan into 4 categories: air (0), skin (4), adipose (1), glandular tissue (2). The interior of the breast is therefore defined up to the accuracy of the segmentation algorithm by categories 1 and 2.

3.2 Sampling of ROIs

In this work we consider the kurtosis of spatial samples from within a single image. Kurtosis is then averaged across multiple images. For both projection mammography and bCT images, regions of interest (ROIs) are selected from within the images. Figure 3 shows the process graphically. In the projection mammograms, the interior of the breast is determined manually by selecting a boundary, and making sure that ROIs are entirely contained inside this area. A total of 50 ROIs at 160 pixels (4.0cm) on a side were sampled randomly from within the interior of each breast. One example of the boundary and location of extracted ROIs is seen in Figure 3A.

For bCT images (and segmented bCT images), the axial range of each 3D image was selected manually to avoid areas of chest wall and narrowing of the breast towards the nipple. There were on average 162 coronal images in the axial range (coefficient of variation 28%) corresponding to an average length of 4.1cm. A total of 50 ROIs were chosen randomly across the axial range and located randomly within the interior of the breast, subject to a check of the segmented images to make sure they had only adipose and glandular segmentation categories (i.e. no air or skin). Each ROI was 128 pixels on a side (4.4cm on average). When an ROI was selected, it was extracted from both the bCT image, and the segmented image. Figure 3B shows the location of coronal ROIs – selected throughout the 3D axial range – on the coronal image closest to the chest wall.

3.3 Computation of SparseNet basis functions

The SparseNet basis functions were obtained by running the SparseNet software [11] on the ROI samples of projection mammograms or bCT images. A single 256 by 256 pixel interior ROI was taken from each of 250 projection mammograms from our database and used to generate image patches for the SparseNet program. The 50 ROIs from 40 bCT scans (a total of 2000 ROIs) were used to generate bCT image patches.

Because of the computational requirements of the SparseNet program, the ROIs were low pass filtered and downsampled by a factor of 2, and image patches were restricted to randomly selected 20 by 20 pixel subregions. These image patches were then whitened by projection onto the first 300 principle components of a large set of patches and then division by the standard deviation of each component. Basis functions were initialized with white noise, and then updated via a stochastic gradient descent algorithm. For display purposes, the basis functions were mapped back into the pixel domain via the inverse of the whitening procedure described above. The kurtosis of these basis functions was evaluated by computing responses on the same ROIs as the Gabor filters after upsampling to the original pixel size. Note that for these purposes, the pixel size of the bCT images was assumed to be the average value of 0.34mm.

4. RESULTS AND DISCUSSION

4.1 Kurtosis of Gabor Filters

Kurtosis results for Gabor filters are shown in Figure 4. Here we have plotted excess kurtosis as defined in Eq. 3 as a function of the center frequency of the octave-bandwidth Gabor filter. Results are plotted for projection mammograms, coronal bCT images, and for binary segmentations of the bCT images. Mammograms generally show increasing kurtosis with increasing spatial frequency. Above 0.50 cyc/mm kurtosis appears to saturate at values near 1. The coronal bCT images show a strong peak in kurtosis at lower frequencies near 0.18 cyc/mm, where observed kurtosis gets as high as 2.07 before decaying to zero. Kurtosis for the segmented bCT images is near the values observed for bCT at the lowest spatial frequencies. However the segmented bCT images continue to increase monotonically at higher spatial frequencies.

Comparing the segmented and non-segmented bCT kurtosis results using a paired comparison *t*-test finds significant differences ($df = 43$, two-sided, $p < 0.05$) at the two lowest frequencies and the three highest frequencies tested. At low spatial frequencies, the bCT images have higher kurtosis than the segmentations. This may be due to properties of the segmentation algorithm or possibly to cupping artifacts in some of the bCT scans. At high spatial frequencies kurtosis of the segmentations consistently increases while that of the bCT images returns to zero. This suggests that image noise, which should have little excess kurtosis, begins to dominate the bCT signal at these frequencies. The idealized sharp edges of the segmentations continue to produce kurtosis in the responses of high-frequency filters in the absence of image noise or limited resolution.

Comparing the kurtosis of the coronal bCT images to the projection mammograms, we find significant differences in two-sample unequal variance *t*-test ($df = 121$, two-sided, $p < 0.05$) at the four lowest and two highest spatial frequencies.

At high spatial frequencies kurtosis is higher in projection mammography images suggesting that the lower noise and higher resolution of the images capture non-Gaussian properties of the tissue somewhat more effectively. At spatial frequencies below approximately 0.25 cyc/mm, the bCT image kurtosis is higher, which by the same logic suggests that these images more effectively capture the non-Gaussian properties of breast tissue. If this logic holds, then we night expect better performance in detecting abnormalities in the frequencies with higher kurtosis. This would predict better performance detecting fine structure such as microcalcifications using projection mammography, and better performance detecting gross structural abnormalities such as masses using bCT.

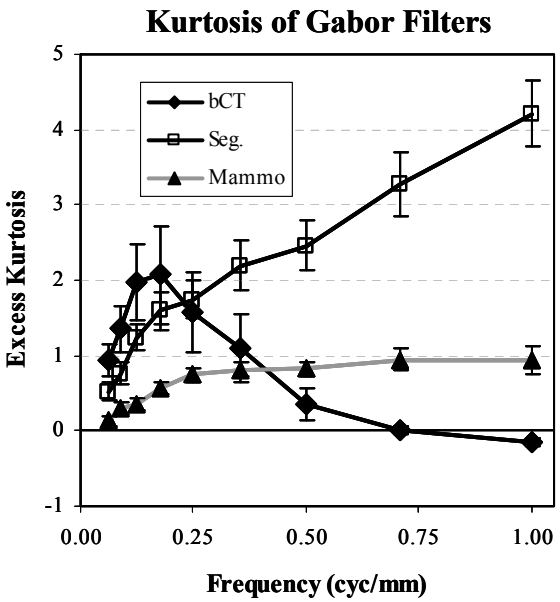

Figure 4. Spatial Frequency Dependence of Kurtosis. Excess kurtosis for coronal breast CT images (bCT), segmented bCT images (Seg.) and projection mammograms (Mammo) are plotted as a function of the center frequency of Gabor patches. Excess kurtosis is computed across 50 ROIs drawn at random from within a case, and then averaged across 6 orientations. Error bars represent ±1 se across cases.

4.2 SparseNet Basis Functions

Figure 5 shows some of the basis functions found using the SparseNet software on the mammography and bCT image sets. The basis functions are ordered by considering each basis function as a filter, and ordering them by the kurtosis obtained in the projection mammography or bCT image data sets. Figure 5A shows the first 100 of 600 total basis functions for each set. The mammography basis functions appear to be mostly Gabor-like, but they appear to be highly elongated in the direction orthogonal to the oscillation. This suggests that they are well suited to represent long narrow linear features in the images, such as Cooper's ligaments or other fibrous tissue.

Figure 5B shows the basis functions derived from coronal bCT images. The initial 70 or so most kurtotic of these basis functions tend to resemble Gabor filters, but subsequent less kurtotic basis functions (including nearly all of the 500 basis functions not shown) lose the appearance of any compact spatial structure. The Gabor-like basis functions appear to be tuned to lower spatial frequencies than the mammography basis functions (more on this topic below), and they are not as elongated in the orthogonal direction. The unstructured basis functions mostly have the appearance of bandpass noise.

To compare with the results using Gabor filters, we need to assign a spatial frequency to the SparseNet-derived filters. We accomplish this by computing the power spectrum of each filter, and then averaging the power as a function of the radial distance to the origin within bins whose size is determined by the frequency sampling. The highest average frequency is then assigned as the center frequency of the filter. Figure 6 shows this process.

Figure 7 shows a plot of center frequency and kurtosis that is similar in character to Figure 4 describing Gabor-filter results. Plotted are the center frequency and kurtosis of the 20 basis functions with the highest kurtosis in each group. The mammography basis functions are spread around an average center frequency of 0.47 cyc/mm with an average kurtosis of 1.18. By contrast, bCT basis functions are clustered more tightly about an average center frequency of 0.16 cyc/mm with an average kurtosis of 1.74. The high kurtosis of the top 20 basis functions of the bCT images relative to the mammography basis functions holds only at the highest kurtosis. For example, the median kurtosis across all 600 basis functions for bCT images is -0.15 while the median across the mammography basis functions in 0.52.

These results, along with the Gabor-filter results, provide convergent evidence that breast CT images are capturing non-Gaussian features of breast tissue at lower spatial frequencies, while the mammography is more effective at capturing non-Gaussian tissue properties at higher spatial frequencies.

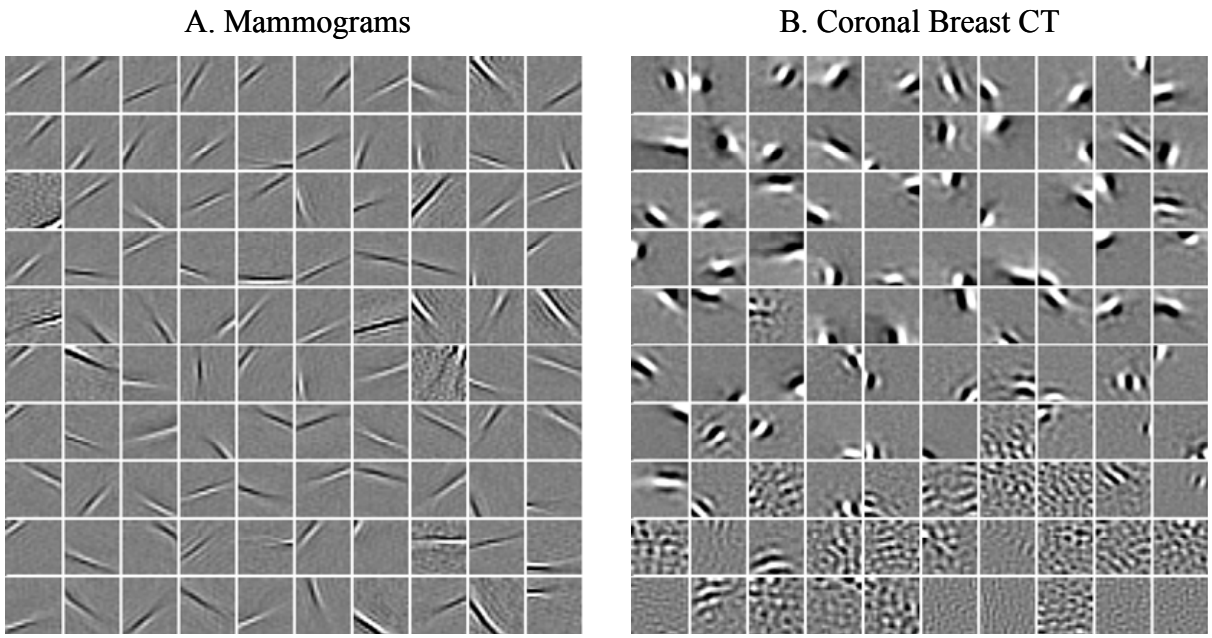

Figure 5. Sparse Basis Functions. Results of the sparse basis optimization procedure for the mammogram data set (A) and bCT data set (B). The 100 most kurtotic basis functions (600 total) are ordered (left to right, top to bottom) by decreasing kurtosis. Note that the 20 by 20 pixel ROIs represent different physical sizes (10.0mm mammography; 13.7mm bCT).

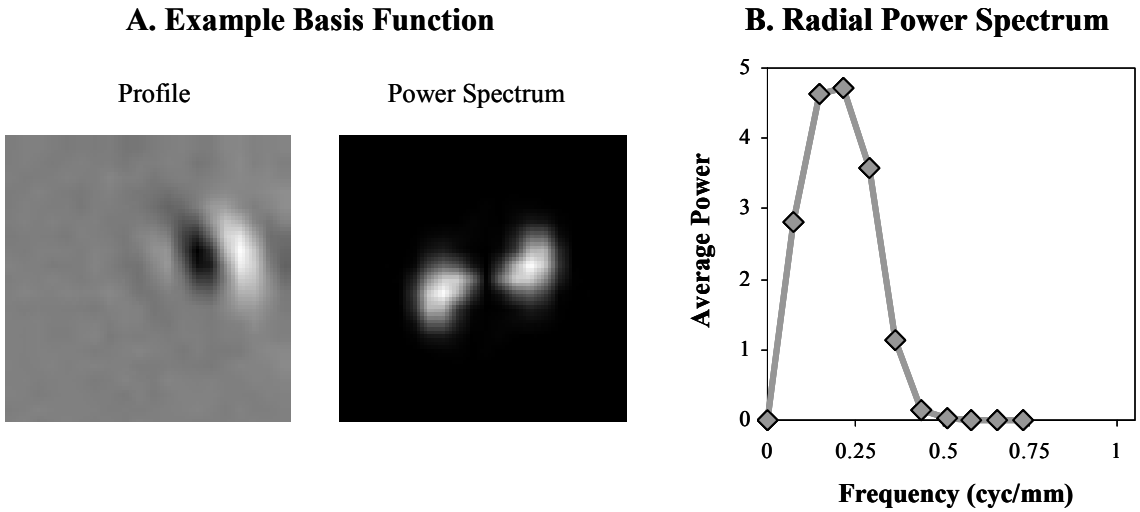

Figure 6. Basis Function Center Frequencies. Each Basis function (example in A left side) is transformed to a power spectrum (A, right side) via the FFT. The center frequency of the basis function (B) is defined as the radial frequency with the highest average spectral power.

5. CONCLUSIONS

We find excess kurtosis across a broad range of spatial frequencies in both projection mammography and coronal bCT images. While the average kurtosis values we find are somewhat less than those reported for calibrated photographs of the world (i.e. "natural scenes"), they nonetheless represent a significant departure from Gaussian statistics. The work of Burgess and others have shown that the power spectrum of breast anatomy in diagnostic images is well described by a

power law [4, 10]. Our findings show quantitatively that higher-order statistics – not captured in a power spectrum – are present and distributed across spatial frequencies in a manner dependent on the imaging modality.

For projection mammograms, the kurtosis of octave-bandwidth Gabor filters increases with spatial frequency to approximately 0.5 cyc/mm, where it saturates at observed values of 0.94 to 0.95. The coronal bCT images exhibit a peak at in kurtosis at 0.18 cyc/mm where an average kurtosis of 2.1 is observed. In addition to using octave bandwidth Gabor functions, we have used the SparseNet approach to investigate the form of filters that emerge naturally from the different types of images. SparseNet optimizes an over-complete set of basis functions used to represent the images under a penalty that rewards sparse representations. A spatial-frequency and kurtosis analysis of the SparseNet basis functions for projection mammograms and coronal bCT images is qualitatively similar to the results with Gabor function. Basis functions derived from projection mammograms cover a broad range of center frequencies about the average of 0.47 cyc/mm, while the basis functions derived from bCT images are confined to low spatial frequencies with an average of 0.18 cyc/mm. The average kurtosis of the basis functions is roughly in accordance with the Gabor functions as well.

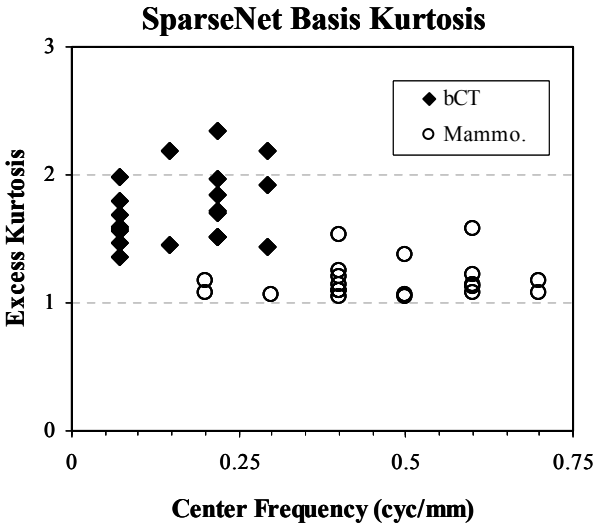

Figure 7. Kurtosis comparison of Sparse Basis functions. The center frequency of the power spectrum and kurtosis are plotted for the 20 SparseNet basis functions with the highest kurtosis.

These results suggest that at lower frequencies, roughly the scale of a mass, the linear filters applied to bCT images more directly access the non-Gaussian sources of variability in the tissue than in standard projection mammograms. However, it remains to be seen if this will translate into a more accurate diagnosis of an abnormal mass.

ACKLOWLEDGMENTS

This work was supported by the NIH through grant R01-EB002138.

REFERENCES

1 H.L. Kundel and G. Revesz, "Lesion conspicuity, structured noise, and film reader error," *Am. J. Roentgenol*. 126:1233–1238, 1976.

2 H. H. Barrett, "Objective assessment of image quality: effects of quantum noise and object variability," *J. Opt. Soc. Am. A* 7, 1266–1278, 1990.

3 F.O. Bochud, J.F. Valley, F.R. Verdun, C. Hessler, and P. Schnyder, "Estimation of the noisy component of anatomical backgrounds," *Med Phys*. 26(7):1365-70, 1999.

4 A.E. Burgess, F.L. Jacobson, and P.F. Judy, "Human observer detection experiments with mammograms and power-law noise," *Med Phys*, 28(4):419-37, 2001.

5 A.E. Burgess, "Mammographic structure: Data preparation and spatial statistics analysis," *Proc. SPIE* (K.M. Hanson, Ed.) 3661:642–653, 1999.

6 A.P. Pentland, "Fractal-based description of natural scenes," *IEEE Trans. Pattern Anal. Mech. Intell.* **6**:661-673. 1984.

7 D.L. Ruderman and W. Bialek, "Statistics of natural images: Scaling in the woods," *Phys Rev Lett*. 73(6):814-817,1994.

8 A. van der Schaaf, and J.H. van Hateren, "Modelling the power spectra of natural images: statistics and information," *Vision Research* **36**:2759–70, 1996.

[9] R.M. Nishikawa, E. Engstrom, and I. Reiser, "Comparison of the Breast Tissue Power Spectrum for Mammograms, Tomosynthesis Projection Images, and Tomosynthesis Reconstruction Images" Presented at *RSNA* Chicago, IL; Nov. 26th, 2007.
[10] K.G. Metheany, C.K. Abbey, N. Packard, and J.M. Boone, "Characterizing anatomical variability in breast CT images," *Med Phys*. 35(10):4685-94, 2008.
[11] B.A. Olshausen and D.J. Field, "Emergence of simple-cell receptive field properties by learning a sparse code for natural images," *Nature*, 381(6583):607-9, 1996.
[12] B.A. Olshausen and D.J. Field, "Sparse coding with an overcomplete basis set: a strategy employed by V1?" *Vision Res*. 37(23):3311-25, 1997.
[13] B.A. Olshausen and D.J. Field, "Sparse Coding of Sensory Inputs" *Cur. Opin. Neurobiol*, 14: 481-487, 2004.
[14] A.J. Bell and T.J. Sejnowski, "The "independent components" of natural scenes are edge filters," *Vision Res*. 37(23):3327-38, 1997.
[15] J.M. Boone, K.K. Lindfors, C.S. Beatty, and J.A. Seibert, "A breast density index for digital mammograms based on radiologists' ranking," *J Digit Imaging*. 11(3):101-15, 1998.
[16] J.M. Boone, T.R. Nelson, K.K. Lindfors, and J.A. Seibert, "Dedicated breast CT: radiation dose and image quality evaluation," *Radiology*, 221(3):657-67, 2001.
[17] J.M. Boone, N. Shah, and T.R. Nelson, "A comprehensive analysis of DgN(CT) coefficients for pendant-geometry cone-beam breast computed tomography," *Med Phys*, 31(2):226-35, 2004.
[18] J.M. Boone, A.L. Kwan, K. Yang, G.W. Burkett, K.K. Lindfors, and T.R. Nelson, "Computed tomography for imaging the breast," *J Mammary Gland Biol Neoplasia*. 11(2):103-11, 2006.
[19] L.A. Shepp and B.F. Logan, "The Fourier reconstruction of a head section," IEEE Trans. Nucl. Sci. 21, 21–43, 1974.
[20] A.L. Kwan, J.M. Boone, K. Yang, and S.Y. Huang, "Evaluation of the spatial resolution characteristics of a cone-beam breast CT scanner," *Med Phys*. 34(1):275-81, 2007.
[21] N. Packard and J.M. Boone, "Glandular segmentation of cone beam breast CT volume images," *Proc. SPIE* (J. Hsieh and M.J. Flynn, Ed.s), 6510(651038):1-8, 2007.
[22] T.R. Nelson, L.I. Cerviño, J.M. Boone, and K.K. Lindfors, "Classification of breast computed tomography data," *Med Phys*. 35(3):1078-86, 2008.